

# Dramatically Enhanced Photoluminescence from Femtosecond Laser Induced Micro-/Nanostructures on MAPbBr<sub>3</sub> Single Crystal Surface

Jun Xing, Xin Zheng, Zhi Yu, Yuhao Lei, Lei Hou, Yuting Zou, Chen Zhao, Bin Wang, Haotian Yu, Dexin Pan, Yuechen Zhai, Jinluo Cheng, Ding Zhou, Songnan Qu, Jianjun Yang, Rashid A. Ganeev, Weili Yu,\* and Chunlei Guo\*


Single crystal perovskites are used in solar cells, photodetectors, and other devices due to their excellent light absorption and carrier transport characteristics. However, for light-emitting applications, photoluminescence (PL) is usually weak for MAPbBr<sub>3</sub> (MA = CH<sub>3</sub>NH<sub>3</sub><sup>+</sup>) single crystals (MBSCs) compared with their polycrystalline counterpart. Therefore, developing novel techniques to process MBSCs with different morphologies for PL-related applications is greatly needed. The current strategies for making perovskite crystals are mostly based on bottom-up method (chemical synthesis and assembling). Here, an easy method to achieve top-down fabrication of MBSCs, i.e., femtosecond laser processing MBSC surface by controlling the laser parameters is demonstrated. The femtosecond laser processing technology can achieve two orders of magnitude enhancement under ambient conditions in PL. In addition, the processed regions also show three times enhancement in PL under nitrogen environment. It is assumed that this is mainly due to the texture based on photon recycling and light out-coupling mechanism, and the passivation of surface recombination centers on MBSC. This study not only provides a convenient top-down strategy to achieve a range of morphological micro-/nanostructures with enhanced PL on MBSC surface, but also paves the way for applications of MBSCs in light emitting or PL imaging devices.

## 1. Introduction

Due to perovskites' unique crystalline and electronic structure, AMX<sub>3</sub> (A = organic or inorganic cation, M = metal cation, and X = halogen anion) structures have excellent photoelectric properties and have been applied to various optoelectronic devices such as solar cells,<sup>[1–3]</sup> light-emitting diodes (LED),<sup>[4–6]</sup> lasers,<sup>[7–9]</sup> field-effect transistors,<sup>[10–12]</sup> and photodetectors.<sup>[13–15]</sup> Up to now, the most widely utilized perovskites include polycrystalline thin films,<sup>[16–18]</sup> nanowires,<sup>[19–21]</sup> nanosheets,<sup>[22,23]</sup> nanorods,<sup>[24,25]</sup> quantum dots,<sup>[26,27]</sup> and bulk single crystals,<sup>[28–31]</sup> and other morphologies. Among all morphologies, the perovskite bulk single crystal has the most excellent carrier transportation properties due to minimal recombination centers and grain boundaries. For example, a carrier diffusion length exceeding 175 μm in MAPbI<sub>3</sub> single crystal has been reported,<sup>[32]</sup> indicating high performance of perovskite single crystal in applications such as solar cells

J. Xing, X. Zheng, Dr. Z. Yu, Dr. L. Hou, Y. Zou, C. Zhao, B. Wang, Dr. J. Cheng, Prof. J. Yang, Prof. R. A. Ganeev, Prof. W. Yu, Prof. C. Guo  
The Guo China-US Photonics Laboratory  
State Key Laboratory of Applied Optics  
Changchun Institute of Optics, Fine Mechanics and Physics  
Chinese Academy of Sciences  
Changchun 130033, P. R. China  
E-mail: weili.yu@ciomp.ac.cn; chunlei.guo@rochester.edu  
J. Xing, X. Zheng, Y. Zou, C. Zhao, B. Wang, Y. Zhai  
University of Chinese Academy of Sciences  
Beijing 100049, P. R. China  
Y. Lei  
Institute of Modern Optics  
Nankai University  
Tianjin 300071, P. R. China

H. Yu, D. Pan  
College of Optical Science and Engineering  
Zhejiang University  
Hangzhou 310027, P. R. China  
Y. Zhai, Dr. D. Zhou, Prof. S. Qu  
State Key Laboratory of Luminescence and Applications  
Changchun Institute of Optics, Fine Mechanics and Physics  
Chinese Academy of Sciences  
Changchun 130033, P. R. China  
Prof. C. Guo  
The Institute of Optics  
University of Rochester  
NY 14627, USA

 The ORCID identification number(s) for the author(s) of this article can be found under <https://doi.org/10.1002/adom.201800411>.

DOI: 10.1002/adom.201800411

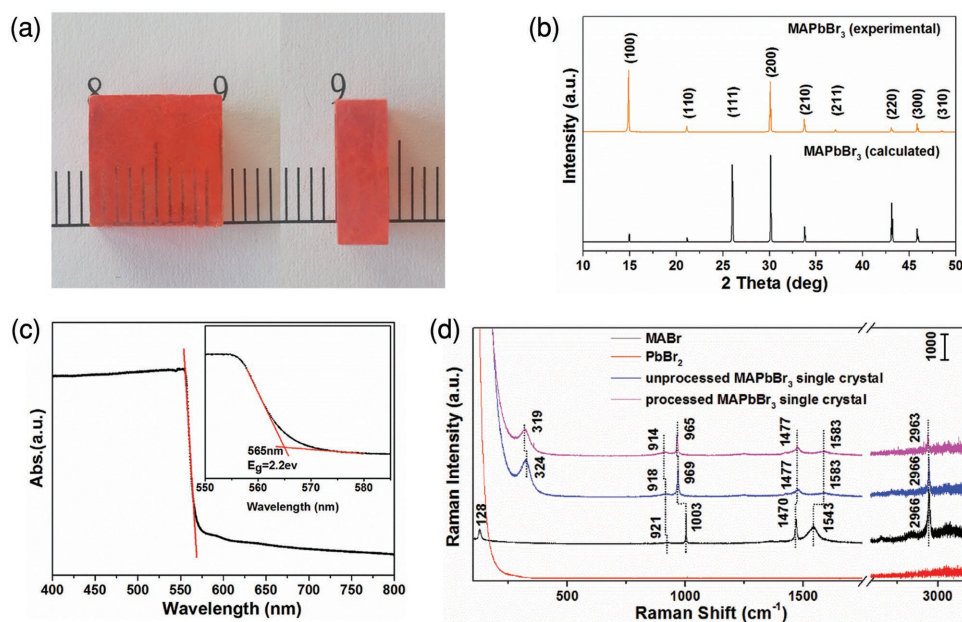


**Figure 1.** Optical image and characterization of MBSC. a) Optical image of MBSC synthesis by ITC method. The dimensions are 10 mm × 9 mm × 4 mm. b) Experimental and calculated powder X-ray diffraction pattern for MBSC. c) Absorption spectra of MBSC. Inset: absorption spectra at the turning point with calculated bandgap energy. d) Raman spectra of MABr, PbBr<sub>2</sub>, unprocessed MBSC, and processed MBSC. All samples were measured in air at room temperature. The probe laser wavelength is 785 nm.

and photodetectors.<sup>[33,34]</sup> However, for light emitting application, studies have shown that the quantum yield of MAPbBr<sub>3</sub> nanoplatelets can reach 85%, much higher than single crystals.<sup>[35]</sup> For example, the external quantum efficiency of LEDs based on MAPbBr<sub>3</sub> quantum dots has reached 8.53%,<sup>[36]</sup> but light-emitting devices based on MBSCs are rarely reported. MBSCs have been found to possess PL properties that are strongly affected by the external environmental factors such as moisture and oxygen level in air.<sup>[37,38]</sup> So strategies that can manually control the surface morphology of MBSC are very necessary for MBSC research.

The bottom-up (chemical synthesis and assembling) methods have limited morphological controllability in synthesizing processes. However, top-down (physical) processing of MBSCs can be controlled in real time and achieve dynamic monitoring, thus improving the PL efficiency. Currently, various approaches such as electron beam lithography, nanoimprint lithography, and masking techniques have been used for material modification.<sup>[39]</sup> However, those modification processes inevitably include hazardous chemical solutions, direct contact processing, and imperfect etching, which result in degradation and destruction of MBSCs.<sup>[40]</sup> Femtosecond laser processing is a novel method that can be used to directly process MBSCs with advantages such as noncontact processing, high processing precision, maskless 3D processing, negligible thermal diffusion effect, and applicability to a wide range of materials.<sup>[41,42]</sup>

In this paper, we apply femtosecond laser processing technology to the surface modification of MBSCs. For the first time, we achieved the surface patterning on the MAPbBr<sub>3</sub> single crystals by femtosecond laser and observed dramatically enhanced PL in the processed region. We discussed the effects of different

laser parameters (laser intensity and scan speed) on the surface morphology of MBSCs and proposed a mechanism for such morphology changes. A patterned word, “CIOMP,” abbreviation of Changchun Institute of Optics, Fine Mechanics and Physics, is directly written by femtosecond laser on the surface of MBSCs and shows significant PL enhancement. We demonstrate that the processed region shows two orders of magnitude PL enhancement in air and three times enhancement under nitrogen ambience compared to unprocessed regions. Furthermore, we assume that the PL enhancement is mainly originated from the texture based on photon recycling and light out-coupling mechanism, and the passivation of surface recombination centers on the MBSC micro-/nanostructure surfaces (texture).

## 2. Results and Discussions

### 2.1. Synthesis and Characterization of MBSC

MBSC was grown from the inverse temperature crystallization (ITC) method detailed in Ref. <sup>[28]</sup> with minor modifications, which yielded a crystal with 10 mm (length) × 9 mm (width) × 4 mm (thickness), as shown in **Figure 1a**. In **Figure S1a** in the Supporting Information, a scanning electron microscope (SEM) image of the MBSC shows a flat and smooth surface without any recombination centers or grain boundary. Energy dispersive spectrometry (EDS) used to map the dotted-line region in **Figure S1b** in the Supporting Information shows uniform elemental distributions of bromide, lead, carbon, and nitrogen, respectively. The EDS spectra also show their peak distribution of these four elements in the mapping area in **Figure S1c** in the

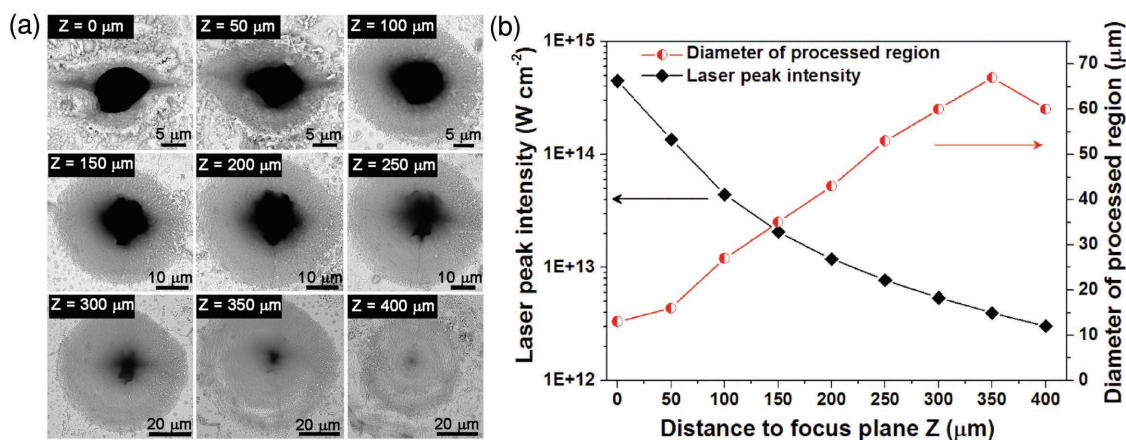


**Figure 2.** Relationship between laser processing parameters and diameter of processed region. a) SEM images of the laser processed region under different distances  $Z$  ( $\mu\text{m}$ ). b) Relationship between both peak laser intensity and diameter of processed region with  $Z$  ( $\mu\text{m}$ ) under 5.4 mW laser power.

Supporting Information. Powder X-ray diffraction (XRD) result in Figure 1b shows cubic structure and is in good agreement with the calculated result of the  $\text{MAPbBr}_3$  single crystals model. The absorption spectra of the MBSC in Figure 1c shows a cut-off wavelength at around 565 nm, where the band gap energy ( $E_g$ ) can be calculated to be about 2.2 eV. Figure 1d shows the Raman spectra of  $\text{MABr}$ ,  $\text{PbBr}_2$ , and MBSC before and after the laser processing (peak laser intensity of  $2.4 \times 10^{12} \text{ W cm}^{-2}$  and scanning speed of  $0.01 \text{ mm s}^{-1}$ ) without any spectral correction or normalization. For  $\text{MABr}$ , several characteristic peaks located at 128, 921, 1003, 1470, 1543, and 2966  $\text{cm}^{-1}$ , are observed in its spectra. The Raman spectra of  $\text{PbBr}_2$  material have characteristic peaks at 105  $\text{cm}^{-1}$  as shown in Figure S2 in the Supporting Information. The single characteristic peaks in  $\text{MABr}$  and  $\text{PbBr}_2$  do not appear in MBSC (324, 918, 969, 1477, 1583, and 2966  $\text{cm}^{-1}$ ). We can thus conclude that  $\text{MABr}$  and  $\text{PbBr}_2$  have been completely converted to MBSC. The characterization of the MBSCs shows good crystalline structure.

## 2.2. Femtosecond Laser Processing and Formation of Micro-/ Nanostructures

Our femtosecond laser has a pulse duration of 35 fs with a central wavelength of 800 nm and a horizontal linear polarization. We investigated the effect of peak laser intensity and defocus distance from the MBSC under the laser power of 5.4 mW. A schematic diagram of our experimental setup is shown in Figure S3 in the Supporting Information. All experiments were carried out under ambient conditions. Figure 2a shows the SEM images of laser processed region variation with different focal distances, which indicate the position of the sample surface in front of the focus plane. The distance ( $Z$ ) between an objective lens (4 $\times$ , NA = 0.1) and the sample surface can be precisely controlled by 3D ( $x$ - $y$ - $z$ ) translation stages. With  $Z$  increasing from 0 to 350  $\mu\text{m}$ , the diameter of processed region increases gradually and the diameter of the middle hole shows a decrease tendency. Figure 2b shows the relationship between the peak laser intensity and the distance  $Z$  ( $\mu\text{m}$ ), which correlates an increased diameter of the processed region. The size of

the processed region decreases beyond 350  $\mu\text{m}$  because of the decreased intensity at the interaction surface.

In order to avoid destructive ablation on the surface of MBSC as shown in Figure 2a while exploring the effect of laser scanning speed on surface morphology, we placed the sample at a defocus (450  $\mu\text{m}$  before focus), which corresponds to a peak laser intensity of about  $2.4 \times 10^{12} \text{ W cm}^{-2}$ . The results are shown in Figure 3. When the scanning speed was  $2.5 \text{ mm s}^{-1}$ , some vertical and horizontal ripples only appeared on the scanned region. As the scanning speed slows to  $0.35 \text{ mm s}^{-1}$ , small nanoparticles appeared on the edge of the processed region, which becomes more and more pronounced at  $0.15 \text{ mm s}^{-1}$ . If we reduced the scanning speed further to  $0.1 \text{ mm s}^{-1}$ , an obvious crack appeared in the processed region center and

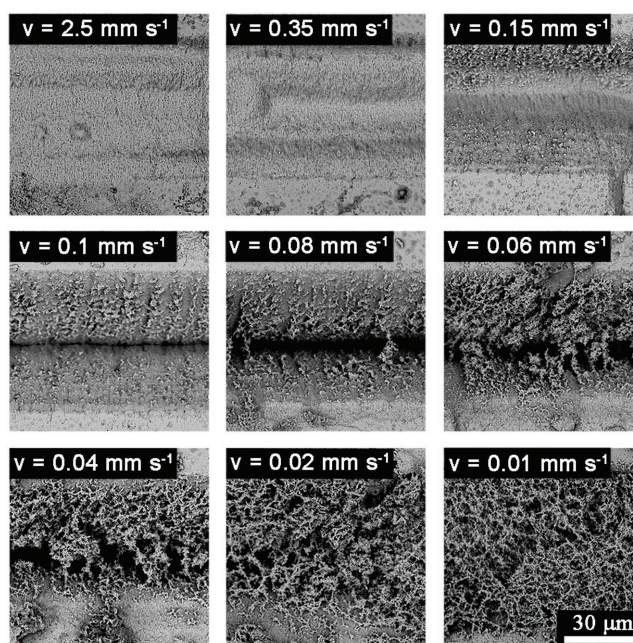


**Figure 3.** SEM images of the laser processed regions at different scanning speeds. The peak laser intensity is kept at  $2.4 \times 10^{12} \text{ W cm}^{-2}$  and the scale bar is 30  $\mu\text{m}$  for all images.



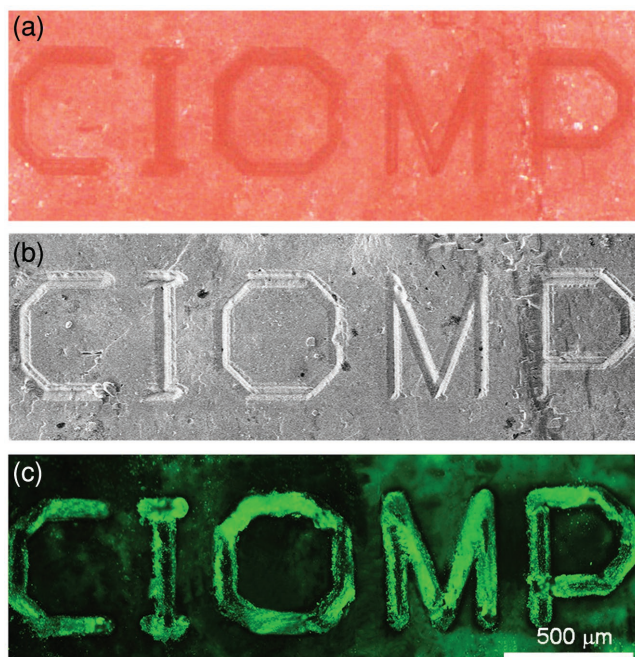


**Figure 4.** Femtosecond laser processing pattern of “CIOMP.” a) Optical image of word “CIOMP.” b) SEM image of word “CIOMP.” c) PL image of word “CIOMP.” The peak laser intensity is kept at  $2.4 \times 10^{12} \text{ W cm}^{-2}$ , and scanning speed is fixed at  $0.2 \text{ mm s}^{-1}$ . The scale bar is the same in all images.

clusters of nanoparticles distribute on both sides. The width of the crack increased as scanning speed decreases from  $0.08$  to  $0.04 \text{ mm s}^{-1}$  and many more micro-/nanorods appeared and gradually overlay the crack. When the scanning speed was fixed at  $0.02 \text{ mm s}^{-1}$ , the crack was completely covered by dendritic micro-/nanostructures that continue to grow much more like a micro-/nanonetwork at  $0.01 \text{ mm s}^{-1}$  (shown in Figure 3). The morphological changes with different scanning speeds are mainly due to the laser energy accumulation, and it can be employed to control morphology on the MBSC surface.

According to the Wagner’s theory,<sup>[43]</sup> formation of various morphologies at different laser scanning speeds is mainly due to the diffusion process of atoms or ions at different temperatures. The diffusion is mainly grain boundary diffusion at low temperatures, sub-boundaries (dislocations) diffusion at moderate temperatures, and lattice diffusion at high temperatures. First, the laser heats the MBSC to melt and generates ripples. Then with increasing temperature, nanoparticles appear on the edge of the laser processed region and spread as a result of the grain boundary diffusion. Finally, most nanoparticles tend to become micro-/nanorods and form a network structure due to the sub-boundary (dislocation) diffusion.

In addition, the simple and fast processes can be achieved on the surface of MBSC by directly laser processing. As shown in Figure 4, the word, “CIOMP,” was written directly with the peak laser intensity of  $2.4 \times 10^{12} \text{ W cm}^{-2}$  and scanning speeds of  $0.2 \text{ mm s}^{-1}$  without any damages outside of the processed region due to no obvious thermal-diffusion effect. The MBSC shows green PL under  $488 \text{ nm}$  laser excitation in Figure 4c. An interesting phenomenon is that the PL in the processed region

is much brighter than that in the unprocessed region, even at same excitation power, which indicates that the laser processing can significantly enhance PL of the MBSC surface. Besides that, a red shift of several feature peaks ( $319, 914, 965,$  and  $2963 \text{ cm}^{-1}$  corresponding to torsional mode [ $\tau(\text{MA})$ ], rocking modes [ $\rho(\text{MA})$ ], stretching mode [ $\nu(\text{C-N})$ ], and symmetric stretching mode [ $\nu_s(\text{NH}_3^+)$ ] respectively)<sup>[44]</sup> in the Raman spectra of MBSC is also observed in Figure 1d. This indicates that the thermal effect of the laser energy slightly alter the molecular pattern of MA, C–H, and  $\text{NH}_3^+$ , and may not influence the original cubic phase lattice of the MBSC surface.<sup>[44]</sup>

### 2.3. PL of MBSC Before and After Femtosecond Laser Processing

In order to explore the exact processed depth and edge morphology of the MBSC under  $2.4 \times 10^{12} \text{ W cm}^{-2}$  peak laser intensity and  $0.01 \text{ mm s}^{-1}$  scanning speed, we performed a 3D topography measurement on the edge of processed region. As shown in Figure S4 in the Supporting Information, the processed region is V-shaped with a large number of nanoparticles on the edge. The effective processed depth can increase to  $\approx 35 \mu\text{m}$ , and the micro-/nanostructures at the edge can approach  $10 \mu\text{m}$  beyond the edge. In order to understand the influence of the micro-/nanostructures on the PL of MBSC, we chose an processed region ( $2.4 \times 10^{12} \text{ W cm}^{-2}$  peak laser intensity and  $0.01 \text{ mm s}^{-1}$  scanning speed) and unprocessed regions to measure the PL at different depths, from  $0$  to  $-80 \mu\text{m}$ , by setting the unprocessed region’s plane as  $0 \mu\text{m}$  in Figure S5 in the Supporting Information. The SEM image of MBSC clearly shows that the micro-/nanostructures distributed like coral and almost completely covered into V-shaped grooves. As we can see, PL in the processed region shows clearly depth dependence in wide range (from  $D = 0$  to  $-80 \mu\text{m}$ ). When  $D = 0 \mu\text{m}$ , the PL intensity is highest. As the depth increases ( $D = 0$  to  $-80 \mu\text{m}$ ), the PL intensity decreases significantly till almost negligible, as can be seen from the intensity scale. At different depths, the PL intensity of micro-/nanostructures is apparently higher than that of the bulk PL. When the depth is larger than  $-20 \mu\text{m}$ , uniform weak PL dominates.

To further clarify the effect of micro-/nanostructures on PL enhancement, we focused PL at narrow range of depths (from  $0$  to  $-1.5 \mu\text{m}$ ) around the MBSC surface. The result presented in Figure 5a shows clearly that PL intensity in the processed region is much higher than in the unprocessed region in different layers. Moreover, with the depth of the focus plane ranging from  $0$  to  $-1.5 \mu\text{m}$ , the bright area gradually extend to the entire laser processed region, which may result from the superposition of PL from the micro-/nanostructures. As shown in Figure 5b, the micro-/nanostructures cover the upper part of the trench and extend about  $7 \mu\text{m}$  beyond the unprocessed region. To prove the existence of PL superposition, we select a series of positions located in the processed and unprocessed regions to measure the PL at different depths from  $10$  to  $-50 \mu\text{m}$  (shown in Figure 5c). We can calculate that the focal diameter size is  $1 \mu\text{m}$  and focal depth is  $13 \mu\text{m}$ , with the excitation laser ( $\lambda = 473 \text{ nm}$ ) under objective lens ( $50\times, \text{NA} = 0.5$ ). For the processed region, the micro-/nanostructures are generally

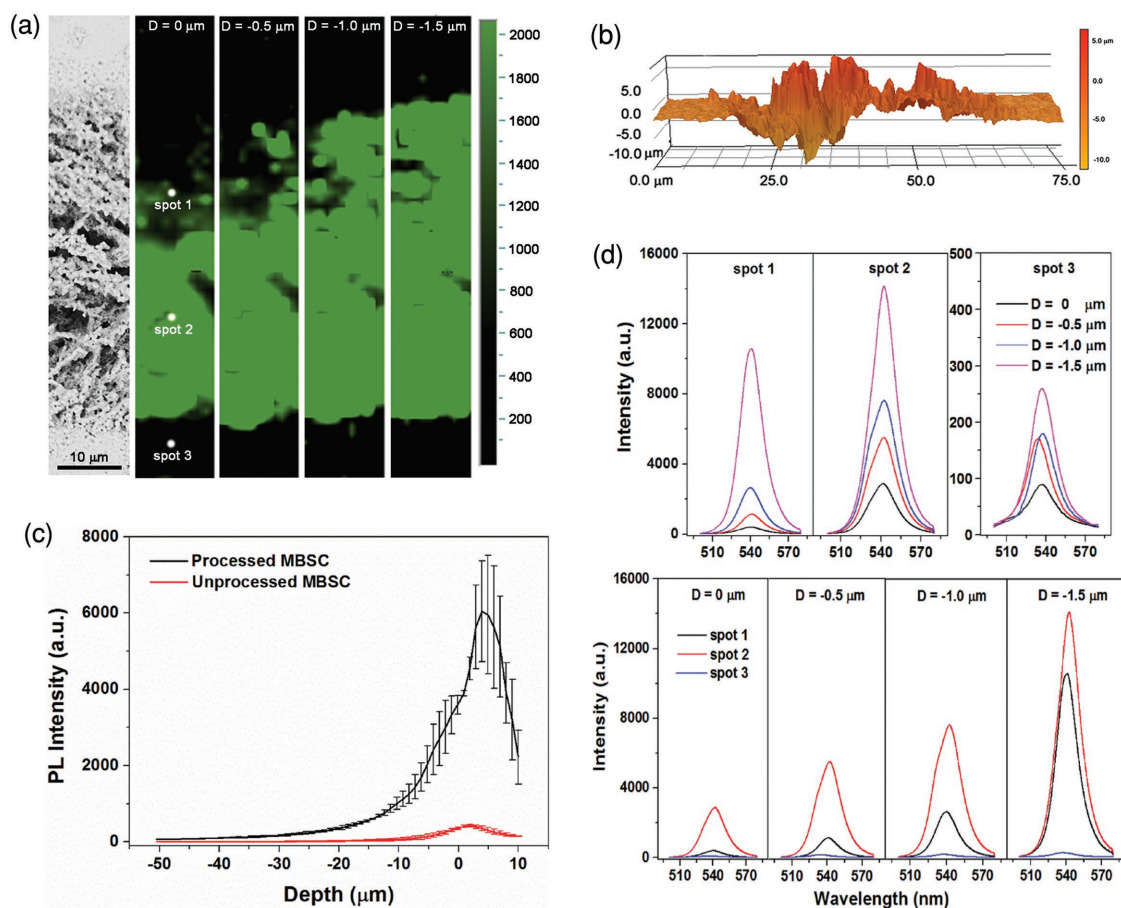


**Figure 5.** SEM image, PL intensity distribution, 3D pseudo color plot, PL variation with depth and PL spectra of MBSC in air. a) SEM image (left) and general caption PL intensity distribution on processed MBSC at different depths (from 0 to  $-1.5 \mu\text{m}$ ) in air at room temperature. b) 3D pseudo color plot of the depth variation on selected region. c) Relationship between PL intensity of processed and unprocessed region and different depths. d) Comparison of PL spectra at different locations and different depths. The excitation laser wavelength is 473 nm.

higher than the  $0 \mu\text{m}$  plane, thus the PL intensity we measured in the processed region from 0 to  $-1.5 \mu\text{m}$  is, in fact, mainly the PL of micro-/nanostructures above 0 plane. Due to sufficient micro-/nanostructures and excitation above threshold, the PL intensity in the processed region shows an additive phenomenon and becomes stronger and stronger from 0 to  $-1.5 \mu\text{m}$ . In addition, the PL intensity of each selected point, shown in Figure 5a, gradually increases as the depth down in Figure 5d, and we find that PL intensity in the processed region is two orders magnitude higher than that of the unprocessed regions on the MBSC surface. Although the PL intensity of a specific monolayer is difficult to be calculated, we still could conclude that the PL enhancement is due to the existence of the micro-/nanostructures. It is noteworthy that there is no obvious shift in PL wavelength ( $\lambda = 540 \text{ nm}$ ) in processed region, which indicates that the elements of MBSCs system in processed region remain the same. From the EDS mapping results in Figure S6 in the Supporting Information, the four elements (bromide, lead, carbon, and nitrogen) of the MBSC are evenly distributed, which is consistent with the SEM results.

To confirm that the micro-/nanostructures formed by the laser processing are stable in different atmospheres, we

measured the PL intensity of the processed region in  $\text{N}_2$ , and the results are shown in Figure 6. PL is significantly stronger in the processed region under  $\text{N}_2$  environment, demonstrating that the micro-/nanostructures are contribute to the PL enhancement. In addition, the PL spectra of the selected points at different depths still shows that PL gradually increases with the focused plane dropping down in Figure 6b. PL intensity in the processed region is two to three times greater than in the unprocessed region in each focused layer, but overall PL intensity in nitrogen is significantly weaker than that in air under the same excitation conditions. The PL spectra in nitrogen is blue shifted from 540 to 518 nm, and the reason for the blue shift can be referenced.<sup>[45,46]</sup> Based on the conclusion of these previously papers, the diminished PL enhancement in nitrogen is related to the lack of moisture and oxygen that can supply electron density to  $\text{Pb}^{2+}$  on MBSC surfaces, due to the loss of bromide,<sup>[37]</sup> which greatly reduces the overall PL intensity. But, micro-/nanostructures in the processed region still showed the PL enhancement, which is believed mainly due to the texture based on photon recycling and light out-coupling mechanism as discussed below.



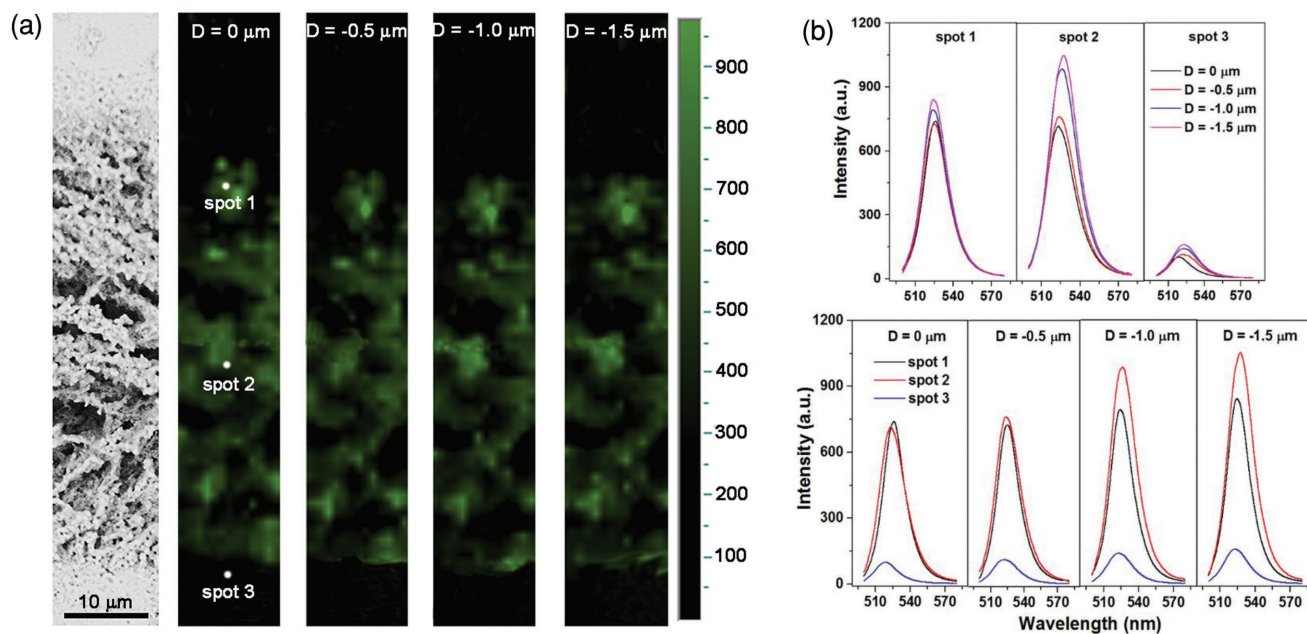


**Figure 6.** SEM image, PL intensity distribution, and PL spectra at different depths of MBSC in  $N_2$ . a) SEM image (left) and general caption PL intensity distribution on processed MBSC at different depths (from 0 to  $-1.5 \mu\text{m}$ ) in nitrogen atmosphere at room temperature. b) Comparison of PL spectra at different locations and different depths. The excitation laser wavelength is 473 nm.

#### 2.4. Exploration on the Mechanism of PL Enhancement

As shown in Figure 7a, we measured the ratio of the surface area to the volume in three regions consisting of two unprocessed regions on the edge and one intermediate processed region. The specific values of the ratio in Table S1 in the Supporting Information demonstrate that the specific surface area of the processed region is about 2.3 times that of the unprocessed region. Furthermore, we also measured the surface roughness of these regions and the specific values of  $R_a$

(arithmetical mean deviation) and  $R_q$  (root mean squared) in Table S2 in the Supporting Information, which shows that the surface roughness of the processed region is more than ten times that of the unprocessed region. From the SEM images in Figure 7b, the coral-like micro-/nanostructures are mainly constituted by micro-/nanorods and nanoparticles around each micro-/nanorods. These nanoparticles, with sizes less than 500 nm, were believed key to the PL enhancement.

We carried out time-resolved photoluminescence to investigate the effect of micro-/nanostructures on MBSC PL lifetime

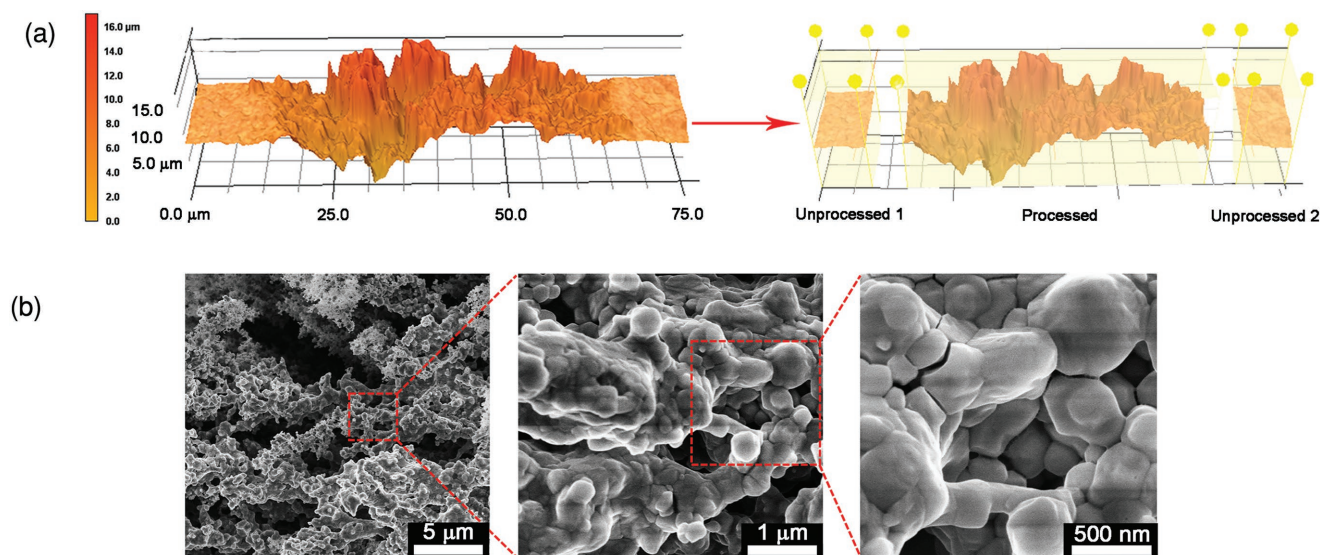


**Figure 7.** 3D pseudo color plot in the processed region and SEM images of micro-/nanostructures. a) 3D pseudo color plot of the topography depth changes in processed and unprocessed regions. b) SEM images of the micro-/nanostructures with  $2.4 \times 10^{12} \text{ W cm}^{-2}$  peak laser intensity and  $0.01 \text{ mm s}^{-1}$  scanning speed in different scales.

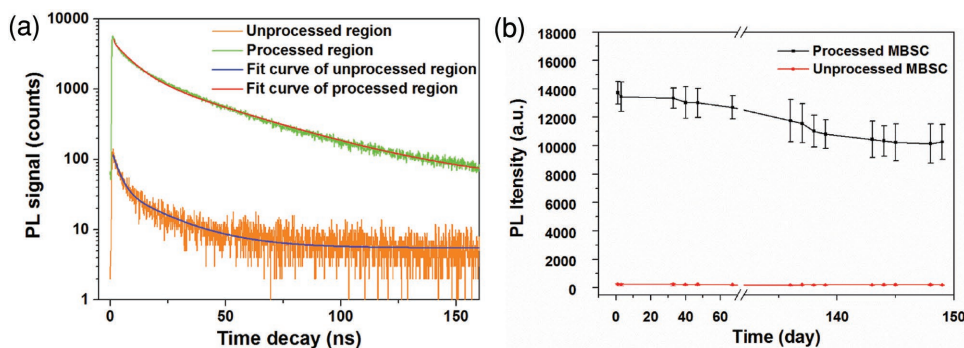


**Figure 8.** The PL decay time traces and the stability of PL enhancement in the processed crystal. a) PL decay time traces in the processed and unprocessed region of MBSC with biexponential fit curve ( $\lambda = 481$  nm). b) The stability of the PL enhancement in the processed and unprocessed region of MBSC.

as shown in **Figure 8a**. The biexponential decay function fitted well to each PL lifetime decay curve and we obtained the lifetime in fast and slow decay pathways. The average PL lifetime for the processed and unprocessed region on MBSC was calculated as shown in Table S3 in the Supporting Information. The PL lifetime in the processed region is twice that of the unprocessed region, which was consistent with previous reports<sup>[4–6,36]</sup> that long PL lifetime can lead to strong luminescence intensity. The long PL lifetime in processed region might be attributed to more surface recombination centers were passivated by moisture and oxygen in the air and lost the ability.<sup>[34–37]</sup> We also measured the stability of the PL enhancement from the processed and unprocessed region as show in **Figure 8b**. For processed MBSC, under ambient conditions, its PL intensity maintained 75% after nearly five months. This indicates that the femtosecond laser-induced micro-/nanostructures can not only achieve dramatically PL enhancement but also survive for a long period of time.

We believed that the enhanced PL enhancement is mainly related to two factors: the laser-induced micro-/nanostructures (texture) which cause photon recycling and light out-coupling enhancement, and the passivation of surface recombination on the MBSC surface. The texture induced by femtosecond laser can increase the roughness of the MBSC surface, which further affects both absorption and emission of photons. For the absorption aspect, it can randomize the angle of the incident excitation light, reduce the reflectivity on the MBSC surface, and achieve more scattering of the excitation light, leading to the enhanced light input-coupling.<sup>[41,47,48]</sup> More incident excitation light can promote high internal photoluminescence quantum yield (PLQY) and boost an efficient photon recycling due to the high refractive index around  $n = 2.4$ .<sup>[49]</sup> The efficient photon recycling can further improve the escape probability of PL photons by increasing its optical density.<sup>[50]</sup> As a result, the PL radiated into the air can be enhanced and the external PLQY can be improved.<sup>[51,52]</sup> For the emission aspect, the texture on the MBSC surface also can randomize the direction of the PL emission (the angle of the total reflection can be calculated around  $25^\circ$ ) and promote photons radiating into the air. It boosts the light out-coupling, leading to enhanced PL intensity and external PLQY.<sup>[50,53–56]</sup>

Passivation effect was believed another key factor for enhanced PL. The micro-/nanostructures induced by femtosecond laser on the MBSC surface have a larger specific surface area, which can adsorb more atoms (such as moisture and oxygen) to donate electron density to excess  $Pb^{2+}$ , which can reduce the excitons quenching caused by  $Pb^{2+}$ .<sup>[36,51]</sup> Therefore, in this condition, more surface recombination centers locate on the nanoparticles in the surface texture can be passivated through the neutralization of excess positive charge to reduce the nonradiation recombination.<sup>[34,36,37,51]</sup> In one sentence, the micro-/nanostructures induced by femtosecond laser pulses on MBSC surfaces can significantly enhance PL intensity, resulting from the surface texture and the passivation of surface recombination centers on MBSC processed region.

### 3. Conclusion

In conclusion, we have demonstrated that femtosecond laser pulses can be used to produce a variety of surface morphologies, such as nanoparticles, micro-/nanorods, or networks, on MBSC surfaces by changing the peak laser intensity and the scanning speed. From the small displacement of the characteristic vibration peak in Raman spectra, the uniform distribution of elements in the EDS mapping and the slight red shift in the center wavelength of the PL, we can conclude that femtosecond laser processing changes mainly the surface morphology, with bulk properties well maintained. In addition, a significant PL enhancement occurred in the processed region with two orders of magnitude greater under ambient conditions and about three times greater than in nitrogen at room temperature. The mechanisms of the PL enhancement was attributed to the laser-induced texture based on photon recycling and light out-coupling mechanism, and the passivation of surface recombination centers on MBSC due to the micro-/nanostructures. We ended with demonstration that this study provides not only a convenient top-down strategy (i.e., femtosecond laser processing technology) to achieve multimorphological micro-/nanostructures on MBSC surfaces, but also a novel idea for achieving MBSC PL enhancement, thus paves the way for applications of MBSCs in the light emitting or PL imaging devices.

## 4. Experimental Section

**Materials:** Methylamine solution (40% aqueous solution, Aladdin), lead bromide (PbBr<sub>2</sub>) (99%, Aladdin), *N,N*-dimethylformamide (DMF) (99.5%, Aladdin), hydrobromic acid (HBr) (40% aqueous solution), ethanol absolute, and diethyl ether were all acquired from Sinopharm Chemical Reagent Co., Ltd) without further purification.

**Synthesis Methylammonium Bromide (MABr):** The MABr was synthesized through the reaction of HBr with methylamine solution and then recrystallized from ethanol absolute and diethyl ether.<sup>[31]</sup> First, HBr acid solution (44 mL) was added into methylamine solution (30 mL) in an ice bath for 2 h with stirring. Then the solvent was removed to recover the white powder by rotary evaporation at 60 °C. Next, the white powder (MABr) was redissolved in ethanol absolute and recrystallized with diethyl ether for three times. Finally, the MABr was collected by filtration and dried at 60 °C in a vacuum for one night.

**Synthesis and Analysis of MAPbBr<sub>3</sub> Single Crystal:** MBSC was grown from 1.5 M solution containing PbBr<sub>2</sub> (0.5505 g, 1.5 mmol) and MABr (0.168 g, 1.5 mmol) in DMF using the inverse temperature crystallization (ITC) method.<sup>[28]</sup> First, the precursor solution was prepared at room temperature in order for these two raw materials to completely dissolve. Then it is filtered by using a PTFE filter with 0.22 μm pore size to get a clear solution. Next, the clear solution was undisturbed kept in an oil bath and the oil temperature was gradually raised to 70 °C for single crystal growth. After 2 h, small single crystals with millimeter dimensions were obtained. Finally, a small single crystal was put into a new precursor solution to continue growth, and after 3 h, we could get a large single crystal with a centimeter size. The powder XRD measurement for MBSC was performed by using a BRUKER D8 FOCUS operated in air at room temperature. The absorption spectra of MBSC were recorded on an Agilent Cary 5000. Energy dispersive spectrometry (EDS) mapping of MBSC was measured by using the Phenom Element Identification application attached to the Phenom Pro-X.

**Femtosecond Laser Micromachining System:** A femtosecond laser micromachining system, where a chirped-pulse amplification of Ti:sapphire laser system (Spitfire Ace, Spectra Physics) was adopted as a light source, delivers the linearly polarized 35 fs laser pulse trains at a repetition rate of 1 kHz with the central wavelength λ = 800 nm, and the maximum average power of ≈7 mJ. For details, please refer to the Figure S3 in the Supporting Information.

**Optical Characterization of MAPbBr<sub>3</sub> Single Crystal:** Raman spectra measurement was conducted by using a HORIBA Scientific Raman spectrometer with a 785 nm laser in air at room temperature. All SEM images of microscopic surfaces on MBSC were obtained from a Hitachi S-4800. PL image of the pattern “CIOMP” was obtained by Nikon ECLIPSE Ti with 486 nm laser excitation in air at room temperature. PL spectra and PL distribution images of MBSC also were obtained by a HORIBA Scientific Raman Spectrometer with 2.55 mW cm<sup>-2</sup> laser intensity at 473 nm in air or in N<sub>2</sub> at room temperature. 3D pseudo color plots, the ratio of surface area to volume, and the surface roughness (R<sub>a</sub> and R<sub>q</sub>) were measured by a KEYENCE VK-X200 3D laser scanning microscope. Time-resolved photoluminescence was measured by a MicroTime 200 Time-resolved Fluorescence Microscope (PicoQuant) with 481 nm laser excitation at 5 MHz repeat frequency at room temperature.

## Supporting Information

Supporting Information is available from the Wiley Online Library or from the author.

## Acknowledgements

This work was supported by the National Key Research and Development Program of China (2017YFB1104700), the Natural Science Foundation of

China (NSFC, 61774155, 61705227, 11774340, 21404015), Jilin Province Science and Technology Department Research Project (20150204019GX, 20160520008JH, 20150519003JH).

## Conflict of Interest

The authors declare no conflict of interest.

## Keywords

femtosecond laser processing, MAPbBr<sub>3</sub> single-crystal, micro-/ nanostructures, photoluminescence enhancement

Received: March 29, 2018

Revised: July 5, 2018

Published online:

- [1] W. L. Yu, F. Li, H. Wang, E. Alarousu, Y. Chen, B. Lin, L. F. Wang, M. N. Hedhili, Y. Y. Li, K. W. Wu, X. B. Wang, O. F. Mohammed, T. Wu, *Nanoscale* **2016**, *8*, 6173.
- [2] H. H. Fang, F. Wang, S. Adjokatse, N. Zhao, J. Even, M. A. Loi, *Light: Sci. Appl.* **2016**, *5*, e16056.
- [3] X. Zhang, X. D. Ren, B. Liu, R. Munir, X. J. Zhu, D. Yang, J. B. Li, Y. C. Liu, D. M. Smilgies, R. P. Li, Z. Yang, T. Q. Niu, X. L. Wang, A. Amassian, K. Zhao, S. Z. F. Liu, *Energy Environ. Sci.* **2017**, *10*, 2095.
- [4] Z. K. Tan, R. S. Mghaddam, M. L. Lai, P. Docampo, R. Higler, F. Deschler, M. Price, A. Sadhanala, L. M. Pazos, D. Credgington, F. Hanusch, T. Bein, H. J. Snaith, R. H. Friend, *Nat. Nanotechnol.* **2014**, *9*, 687.
- [5] A. B. Wong, M. L. Lai, S. W. Eaton, Y. Yu, E. Lin, L. Dou, A. Fu, P. D. Yang, *Nano Lett.* **2015**, *15*, 5519.
- [6] N. N. Wang, L. Cheng, R. Ge, S. T. Zhang, Y. F. Miao, W. Zou, C. Yi, Y. Sun, Y. Cao, R. Yang, Y. Q. Wei, Q. Guo, Y. Ke, M. T. Yu, Y. Z. Jin, Y. Liu, Q. Q. Ding, D. W. Di, L. Yang, G. C. Xing, H. Tian, C. H. Jin, F. Gao, R. H. Friend, J. P. Wang, W. Huang, *Nat. Photonics* **2016**, *10*, 699.
- [7] T. Kondo, T. Azuma, T. Yuasa, R. Ito, *Solid State Commun.* **1998**, *105*, 253.
- [8] B. R. Sutherland, S. Hoogland, M. M. Adachi, C. T. Wong, E. H. Sargent, *ACS Nano* **2014**, *8*, 10947.
- [9] A. Fu, P. Yang, *Nat. Mater.* **2015**, *14*, 557.
- [10] C. R. Kagan, D. B. Mitzi, C. D. Dimitrakopoulos, *Science* **1999**, *286*, 945.
- [11] F. Li, C. Ma, H. Wang, W. J. Hu, W. L. Yu, A. D. Sheikh, T. Wu, *Nat. Commun.* **2015**, *6*, 8238.
- [12] F. Li, H. Wang, D. Kufer, L. L. Liang, W. L. Yu, E. Alarousu, C. Ma, Y. Y. Li, Z. X. Liu, C. X. Liu, N. N. Wei, F. Wang, L. Chen, O. F. Mohammed, A. Fratalocchi, X. G. Liu, G. Konstantatos, T. Wu, *Adv. Mater.* **2017**, *29*, 1602432.
- [13] L. Dou, Y. Yang, J. You, Z. Hong, W. H. Chang, L. Gang, Y. Yang, *Nat. Commun.* **2014**, *5*, 5404.
- [14] H. W. Chen, N. Sakai, A. K. Jena, Y. Sanehira, M. Ikegami, K. C. Ho, T. Miyasaka, *J. Phys. Chem. Lett.* **2015**, *6*, 1773.
- [15] W. Wei, Y. Zhang, Q. Xu, H. T. Wei, Y. J. Fang, Q. Wang, Y. H. Deng, T. Li, A. Gruverman, L. Cao, J. S. Huang, *Nat. Photonics* **2017**, *11*, 315.
- [16] K. Mahmood, B. S. Swain, A. Amassian, *Adv. Energy Mater.* **2015**, *5*, 1500568.



- [17] J. B. Li, Y. C. Liu, X. D. Ren, Z. Yang, R. P. Li, H. Su, X. M. Yang, J. Z. Xu, H. Xu, J. Y. Hu, A. Amassian, K. Zhao, S. Liu, *Adv. Opt. Mater.* **2017**, *5*, 1700102.
- [18] R. Munir, A. D. Sheikh, M. Abdelsamie, H. L. Hu, L. Yu, K. Zhao, T. Kim, O. El Tall, R. P. Li, D. M. Smilgies, A. Amassian, *Adv. Mater.* **2017**, *29*, 1604113.
- [19] D. D. Zhang, S. W. Eaton, Y. Yu, L. T. Dou, P. D. Yang, *J. Am. Chem. Soc.* **2015**, *137*, 9230.
- [20] S. W. Eaton, M. L. Lai, N. A. Gibson, A. B. Wong, L. T. Dou, J. Ma, L. W. Wang, S. R. Leone, P. D. Yang, *Proc. Natl. Acad. Sci. USA* **2016**, *113*, 1993.
- [21] M. L. Lai, Q. Kong, C. G. Bischak, Y. Yu, L. T. Dou, S. W. Eaton, N. S. Ginsberg, P. D. Yang, *Nano Res.* **2017**, *10*, 1107.
- [22] L. Protesescu, S. Yakunin, M. I. Bodnarchuk, F. Krieg, R. Caputo, C. H. Hendon, R. X. Yang, A. Walsh, M. V. Kovalenko, *Nano Lett.* **2015**, *15*, 3692.
- [23] Z. J. Tan, Y. Wu, H. Hong, J. B. Yin, J. C. Zhang, L. Lin, M. Z. Wang, X. Sun, L. Z. Sun, Y. C. Huang, K. H. Liu, Z. F. Liu, H. L. Peng, *J. Am. Chem. Soc.* **2016**, *138*, 16612.
- [24] J. J. Urban, S. Y. Wan, G. Qian, H. Park, *J. Am. Chem. Soc.* **2002**, *124*, 1186.
- [25] H. G. Kim, P. H. Borse, J. S. Jang, C. W. Ahn, E. D. Jeong, J. S. Lee, *Adv. Mater.* **2011**, *23*, 2088.
- [26] F. Zhang, H. Zhong, C. Chen, X. Wu, X. Hu, H. Huang, J. Han, B. Zou, Y. Dong, *ACS Nano* **2015**, *9*, 4533.
- [27] A. R. Kirmani, F. P. G. de Arguer, J. Z. Fan, J. I. Khan, G. Walters, S. Hoogland, N. Wehbe, M. M. Said, S. Barlow, F. Laquai, S. R. Marder, E. H. Sargent, A. Amassian, *ACS Energy Lett.* **2017**, *2*, 1952.
- [28] M. I. Saidaminov, A. L. Abdelhady, B. Murali, E. Alarousu, V. M. Burlakov, W. Peng, I. Dursun, L. F. Wang, Y. He, G. Maculan, A. Goriely, T. Wu, O. F. Mohammed, O. M. Bakr, *Nat. Commun.* **2015**, *6*, 7586.
- [29] P. Shaikh, D. Shi, J. Retamal, A. D. Sheikh, M. A. Haque, C. F. Kang, J. H. He, O. M. Bakr, T. Wu, *J. Mater. Chem. C* **2016**, *4*, 8304.
- [30] W. Peng, J. Yin, K. T. Ho, O. Ouellette, M. De Bastiani, B. Murali, O. El Tall, C. Shen, X. H. Miao, J. Pan, E. Alarousu, J. H. He, B. S. Ooi, O. F. Mohammed, E. Sargent, O. M. Bakr, *Nano Lett.* **2017**, *17*, 4759.
- [31] D. Shi, V. Adinolfi, R. Comin, M. J. Yuan, E. Alarousu, A. Buin, Y. Chen, S. Hoogland, A. Rothenberger, K. Katsiev, Y. Losovyj, X. Zhang, P. A. Dowben, O. F. Mohammed, E. H. Sargent, O. M. Bakr, *Science* **2015**, *347*, 519.
- [32] Q. F. Dong, Y. J. Fang, Y. C. Shao, P. Mulligan, J. Qiu, L. Cao, J. S. Huang, *Science* **2015**, *347*, 967.
- [33] H. H. Fang, R. Raissa, M. Abdu-Aguye, S. Adjokatse, G. R. Blake, J. Even, M. A. Loi, *Adv. Funct. Mater.* **2015**, *25*, 2346.
- [34] J. S. Huang, Y. C. Shao, Q. F. Dong, *J. Phys. Chem. Lett.* **2015**, *6*, 3218.
- [35] Y. Ling, Z. Yuan, Y. Tian, X. Wang, J. C. Wang, Y. Xin, K. Hanson, B. Ma, H. Gao, *Adv. Mater.* **2016**, *28*, 305.
- [36] H. C. Cho, S. H. Jeong, M. H. Park, Y. H. Kim, C. Wolf, C. L. Lee, J. H. Heo, A. Sadhanala, N. Myoung, S. Yoo, S. H. Im, R. H. Friend, T. W. Lee, *Science* **2015**, *350*, 1222.
- [37] H. H. Fang, S. Adjokatse, H. T. Wei, J. Yang, G. R. Blake, J. S. Huang, J. Even, M. A. Loi, *Sci. Adv.* **2016**, *2*, e1600534.
- [38] J. Huang, Y. Yuan, Y. Shao, Y. Yan, *Nat. Rev. Mater.* **2017**, *2*, 17042.
- [39] J. Chen, Y. Wu, X. M. Li, F. Cao, Y. Gu, K. Liu, X. H. Liu, Y. H. Dong, J. P. Ji, H. B. Zeng, *Adv. Mater. Technol.* **2017**, *2*, 1700132.
- [40] C. W. Wang, Y. Y. Dang, Y. H. Su, J. C. Ni, C. C. Zhang, J. W. Li, Y. L. Hu, J. R. Chu, W. H. Huang, D. Wu, X. T. Tao, *IEEE Photonics J.* **2017**, *9*, 2400110.
- [41] A. Y. Vorobyev, C. L. Guo, *Laser Photonics Rev.* **2013**, *7*, 385.
- [42] K. Sugioka, Y. Cheng, *Light: Sci. Appl.* **2014**, *3*, e149.
- [43] C. Wagner, *Z. Phys. Chem.* **1933**, *21B*, 25.
- [44] T. Yin, Y. Fang, X. Fan, B. Zhang, J. L. Kuo, T. J. White, G. M. Chow, J. Yan, Z. X. Shen, *Chem. Mater.* **2017**, *29*, 5974.
- [45] G. Grancini, V. D'Innocenzo, E. R. Dohner, N. Martino, A. R. S. Kandada, E. Mosconi, F. De Angelis, H. I. Karunadasa, E. T. Hoke, A. Petrozza, *Chem. Sci.* **2015**, *6*, 7305.
- [46] J. Yang, Z. Yuan, X. Liu, S. Braun, Y. Li, J. Tang, F. Gao, C. Duan, M. Fahlman, Q. Bao, *ACS Appl. Mater. Interfaces* **2018**, *10*, 16225.
- [47] S. M. Sze, K. K. Ng, *Physics of Semiconductor Devices*, John Wiley & Sons, Inc., Hoboken, NJ **2006**, pp. 134–196.
- [48] A. Y. Vorobyev, C. Guo, *Phys. Rev. B* **2005**, *72*, 195422.
- [49] J. S. Park, S. Choi, Y. Yan, Y. Yang, J. M. Luther, S. H. Wei, P. Parilla, K. Zhu, *J. Phys. Chem. Lett.* **2015**, *6*, 4304.
- [50] J. M. Richter, M. Abdi-Jalebi, A. Sadhanala, M. Tabachnyk, J. P. H. Rivett, L. M. Pazos-Outon, K. C. Godel, M. Price, F. Deschler, R. H. Friend, *Nat. Commun.* **2016**, *7*, 13941.
- [51] M. Abdi-Jalebi, Z. Andaji-Garmaroudi, S. Cacovich, C. Stavarakas, B. Philippe, J. M. Richter, M. Alsari, E. P. Booker, E. M. Hutter, A. J. Pearson, S. Lilliu, T. J. Savenije, H. Rensmo, G. Divitini, C. Ducati, R. H. Friend, S. D. Stranks, *Nature* **2018**, *555*, 497.
- [52] V. Badescu, P. T. Landsberg, *Semicond. Sci. Technol.* **1993**, *8*, 1267.
- [53] L. M. Pazos-Outon, M. Szumilo, R. Lamboll, J. M. Richter, M. Crespo-Quesada, M. Abdi-Jalebi, H. J. Beeson, M. Vrucinic, M. Alsari, H. J. Snaith, B. Ehrler, R. H. Friend, F. Deschler, *Science* **2016**, *351*, 1430.
- [54] Q. Y. Yue, W. Li, F. M. Kong, K. Li, *Adv. Mater. Sci. Eng.* **2012**, *2012*, 985762.
- [55] J. H. Hwang, H. J. Lee, Y. S. Shim, C. H. Park, S. G. Jung, K. N. Kim, Y. W. Park, B. K. Ju, *Nanoscale* **2015**, *7*, 2723.
- [56] S. J. Shin, T. H. Park, J. H. Choi, E. H. Song, H. Kim, H. J. Lee, J. I. Lee, H. Y. Chu, K. B. Lee, Y. W. Park, B. K. Ju, *Org. Electron.* **2013**, *14*, 187.